https://doi.org/10.5194/wes-2026-115
Preprint. Discussion started: 8 July 2026

WIND ENERGY SCIENCE DISCUSSIONS
Open Access

Frequent surface–rotor stability decoupling limits the representativeness of surface-based offshore observations

Valeria Vasquez-Barros[1], Nicola Bodini[3], Seth Zippel[4], Anthony Kirincich[5], and Julie K. Lundquist[1,2]

[1]Department of Mechanical Engineering, Johns Hopkins University
[2]Department of Earth and Planetary Sciences, Johns Hopkins University
[3]Department of Atmospheric and Oceanic Sciences, University of Colorado Boulder
[4]College of Earth, Ocean and Atmospheric Sciences, Oregon State University
[5]Department of Physical Oceanography, Woods Hole Oceanographic Institution

Correspondence: Julie K. Lundquist (Julie.Lundquist@JHU.edu)

Abstract. Understanding atmospheric stability throughout the wind turbine rotor layer is critical for predicting wake evolution, power production, wake steering performance, and structural loading. Here, we use sonic anemometer, profiling lidar, and thermodynamic profiler observations collected from an instrumented barge deployed during June-September 2024 as part of the Third Wind Forecast Improvement Project (WFIP3) campaign off the U.S. northeast coast to evaluate how well near-surface measurements represent atmospheric stability at wind turbine hub height. Surface-based and rotor-layer stability classifications disagree more than 30% of the time, with the dominant decoupling regime characterized by unstable surface conditions beneath a stably stratified rotor layer. The frequency of these decoupling events increases through late summer into fall as hub-height stratification strengthens, while individual events become shorter-lived, indicating frequent transitions between coupled and decoupled states. Decoupling events are characterized by slower wind speeds consistent with weaker turbulent mixing through the marine boundary layer. Surface observations often fail to represent the atmospheric stability experienced by offshore wind turbines during summer marine conditions. Consequently, relying solely on near-surface measurements may underestimate the occurrence of stable rotor-layer conditions that influence wake behavior, offshore wind farm power performance, and estimates of structural loads.

1 Introduction

Atmospheric stability influences the performance of offshore wind turbines by governing turbulence levels, power generation, wake evolution, wake steering effectiveness, and structural loading. Stable atmospheric conditions suppress turbulent mixing, allowing wind turbine wakes to propagate further downstream and increasing wake losses, while unstable conditions enhance mixing and promote wake recovery (Lundquist et al., 2018; Keck et al., 2014; Machefaux et al., 2016). Atmospheric stability also influences the effectiveness of wake steering (Fleming et al., 2017) and can alter fatigue and extreme structural loads experienced by wind turbines (Sathe et al., 2013). Consequently, accurately characterizing atmospheric stability throughout the turbine rotor layer has become a fundamental requirement for offshore wind resource assessment, operational forecasting, wake modeling, and wind farm control.

Despite this importance, atmospheric stability is rarely measured directly throughout the turbine rotor layer. Instead, operational monitoring, numerical weather prediction model validation, and many offshore observational studies characterize atmospheric stability using surface-layer stability metrics. These metrics may include the Obukhov length measured from meteorological towers or buoys sampling the lowest tens of meters. In other cases, the air-sea temperature difference measured in the lowest tens of meters is used in a Richardson Number calculation (Sathe et al., 2011; Djath et al., 2018; Schneemann et al., 2021; Paulsen et al., 2026). Implicit in these approaches is the assumption that near-surface measurements provide a representative description of the atmospheric conditions experienced by modern offshore wind turbines, whose rotor disks now routinely span heights of 100 to 250 m above the ocean surface.

That assumption may not always be valid. During stable marine conditions, turbulence generated near the ocean surface may remain confined to the lowest tens of meters while the atmosphere aloft remains stably stratified. Surface observations may indicate unstable or weakly unstable conditions, even though the turbine rotor layer remains stably stratified. Under these circumstances, measurements commonly used to characterize atmospheric stability for offshore wind applications become unrepresentative of the conditions actually experienced by wind turbines. Such vertical decoupling would lead surface-based observations to underestimate the occurrence of stability regimes that are most relevant for power production, turbulent structural loads, and wake dynamics. Although previous modeling (Rosencrans et al., 2024; Xia et al., 2025) and observational (Cimini et al., 2025; Platis et al., 2022) studies have recognized that surface-layer stability metrics may not fully characterize offshore boundary-layer structure, the frequency, persistence, and meteorological controls of disagreements between surface- and rotor-layer stability have not been quantified using co-located offshore observations.

In this study, we use observations collected during the Third Wind Forecast Improvement Project (WFIP3) from an instrumented barge deployed offshore near the Vineyard Wind wind farm during the summer and early fall of 2024 to evaluate how well surface measurements represent atmospheric stability at turbine hub height. Sonic anemometers mounted on the barge quantify surface-layer stability via the Obukhov Length, while a profiling lidar and infrared thermodynamic profiler provide wind and temperature profiles that allow calculation of the Bulk Richardson number throughout the rotor layer. Comparing these independent measurements allows us to directly quantify when surface observations accurately represent rotor-height stability and when they do not.

To describe these situations, we distinguish between coupled and decoupled stability regimes. Coupled conditions occur when the stability classification is consistent between the surface layer and the rotor layer, whether both are stable or both are unstable. Decoupled conditions occur when the stability classifications differ between the two layers. Of greatest importance for offshore wind energy are periods during which the surface layer is unstable while the turbine rotor layer remains stably stratified, because relying solely on surface observations during these times risks underestimating stable atmospheric conditions that strongly influence wake evolution and turbine performance.

The objectives of this study are therefore to (1) quantify the frequency with which conventional surface observations fail to represent rotor-layer stability, (2) identify the diurnal and seasonal (over the course of the summer and early fall) variability of these decoupling events, (3) characterize the duration and persistence of prolonged decoupling episodes, and (4) discuss the implications for offshore wind measurements, atmospheric model evaluation, and wind farm applications.

The remainder of this paper is organized as follows. Section 2 describes the WFIP3 observational datasets and their processing. Section 3 introduces the stability metrics used to compare surface and rotor-layer atmospheric conditions. Section 4 quantifies how frequently conventional surface observations fail to represent rotor-layer stability, examines the seasonal and diurnal variability of these decoupling events, and characterizes their persistence. Finally, in Section 5, we discuss the implications of these findings for offshore atmospheric measurements, wind farm applications, and future observational and modeling studies.

2 Data

2.1 The Third Wind Forecast Improvement Project (WFIP3)

This study analyzes in situ flux measurements as well as remotely sensed temperature and wind profile observations from the Third Wind Forecast Improvement Project (WFIP3) to classify atmospheric stability within different height intervals (Kirincich et al., 2026; Bodini et al., 2026b). The Wind Forecast Improvement Projects are a series of U.S. Department of Energy-sponsored field campaigns focused on improving weather modeling and forecasting using computational and observational methods. WFIP1 was conducted in the Midwest/central plains (Wilczak et al., 2015) while WFIP2 occurred in the Columbia River Gorge of the Pacific Northwest region of the United States (Shaw et al., 2019; Olson et al., 2019; Wilczak et al., 2019). This third project studied the Marine Atmospheric Boundary Layer (MABL) along the U.S. East Coast (Figure 1) due to the region's opportunity for offshore wind energy production and the accompanying need for forecast improvement (Kirincich et al., 2026; Bodini et al., 2026b; Adler et al., 2026).

The main objectives of WFIP3 were to gather data on the vertical structure of the MABL across different regions along the East Coast to understand its complexity and variability (Kirincich et al., 2026). These findings should help optimize numerical weather model prediction models that can be applied to wind energy (Adler et al., 2026). Six coastal field sites, including the offshore Air-Sea Interaction Tower (Edson et al., 2007; Bodini et al., 2019; Cinquino and Kirincich, 2024), used lidars, radiometers, cloud and precipitation sensors, and surface meteorological stations to characterize the coastal boundary layer, while one temporary far-offshore site, the Barge site, characterized the marine boundary layer.

2.2 Barge Deployment

A unique observational platform, an instrumented barge (Figure 1), was one of WFIP3's innovations. The 46 m by 16.5 m barge was deployed off the coast of Massachusetts and Rhode Island between June and October 2024, 44 km south of Martha's Vineyard in water 52 m deep, to gather extensive data on the MABL (Bodini et al., 2026a; Kirincich et al., 2026) in the vicinity of the Vineyard Wind offshore wind farm. For the prevailing wind direction (southwesterly), the nearest "upwind" land location in New Jersey is approximately 280 km away. The deployment of this barge is of particular interest due to its proximity to many offshore wind farm lease areas. The barge provides the data analyzed in this study.

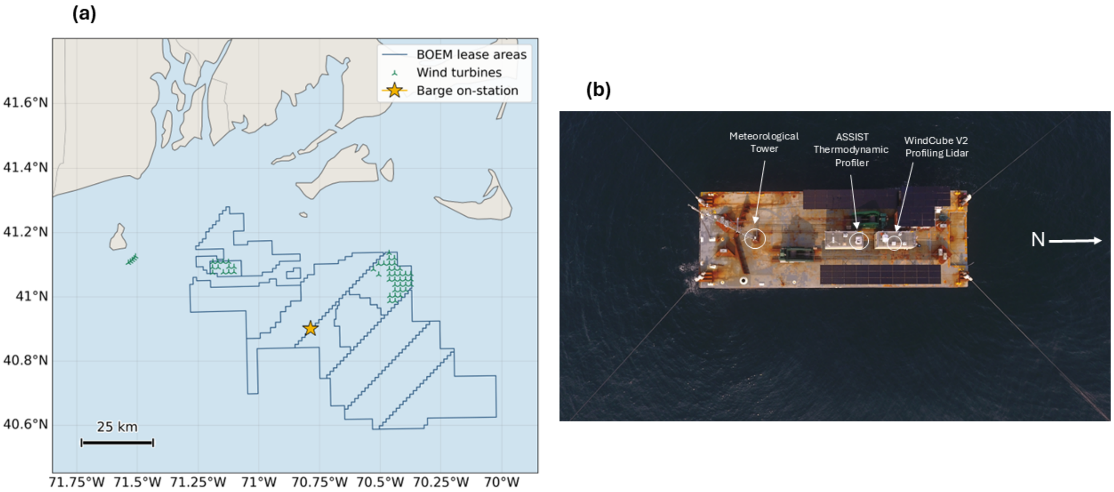

Figure 1. Map (a) of the U.S. Northeast Coast including offshore lease areas, turbines installed by May 2024, and the barge location and photo (b) of moored barge annotating locations of met tower, ASSIST, and lidar. Photo credit Eve Cinquino, WHOI.

Start	End	Days On-Station
05:00 UTC 17 Jun 2024	11:00 UTC 23 Jun 2024	7
05:00 UTC 29 Jun 2024	11:00 UTC 8 Aug 2024	40
06:00 UTC 23 Aug 2024	10:00 UTC 28 Sep 2024	38

Table 1. Dates when the WFIP3 Barge was on-station at 40.901°, -70.787°

The barge was deployed on tation for a total of 85 days, over the 120 day period, as it was recovered and towed to shore for 2 large wave events events (Table 1). During the deployed periods, its 16 instruments document the MABL in the region, collecting wind and thermodynamic data, as well as precipitation profiles, and wildlife information (birds and bats). The most relevant instruments for this study are the profiling lidar, the ASSIST thermodynamic profiler, and the sonic anemometers on the meteorological mast, summarized in Table 2.

2.3 WindCube V2 Profiling Lidar

The WindCube V2 profiling lidar was deployed on the barge to capture vertical profiles of wind speed and wind direction. The lidar measures the Doppler shift in frequency from its laser reflecting off of aerosols and other particles in the flow, and calculates the radial velocity projection onto the four beams projected θ degrees from vertical in the northerly ($v_{r,N}$), easterly

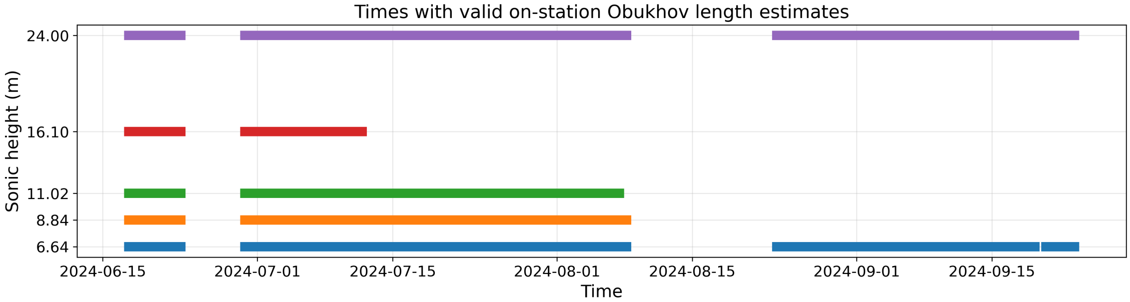

Figure 2. Data availability from the sonic anemometers on the barge. Off-station times have been removed.

Instrument	Variables	Heights Used	Temporal Resolution	Primary Use
3-D sonic anemometers	3-components of wind speed, sonic temperature T_s, turbulence	6.64 m, 24 m	20 Hz or 32 Hz averaged to 20 min	Obukhov length (L)
WindCube V2 profiling lidar	Wind speed, wind direction	40–160 m (20 m spacing)	1 sec averaged to 10 min	winds for Ri
ASSIST infrared spectrometer	Temperature, humidity, pressure	Surface–160m (∼10 m near surface)	10 min	θ_v for Ri
Thermometer	Air temperature	7.87, 10.0 , 16.0 , 23.3 m	1 sec	T profiles

Table 2. Summary of the observations used in this study.

($v_{r,E}$), southerly ($v_{r,S}$), westerly ($v_{r,W}$) directions (Lundquist et al., 2015; Robey and Lundquist, 2022). The lidar assumes horizontal homogeneity, meaning the flow is assumed constant along the measurement scan. The WindCube V2 emits five beams, one in the vertical direction, and four along each of the cardinal directions at an angle $\theta \approx 30°$ off the vertical. A high-frequency inclinometer captured the motion of the barge, and those measurements were used to correct the lidar observations as per the methodology in Krishnamurthy et al. (2023) and Newsom et al. (2024). For this dataset, the WindCube V2 captured vertical wind profiles every 20 meters between 40-300 m altitudes. Since the lowest measured height is 40 meters on the lidar, 40-60 meters is the lowest available level for stability assessment with the lidar. Temporally, velocity profiles were averaged over 10 minutes.

https://doi.org/10.5194/wes-2026-115
Preprint. Discussion started: 8 July 2026

2.4 ASSIST+TROPoe

The Atmospheric Sounder Spectrometer by Infrared Spectral Technology (ASSIST-II by LR Tech Inc.), hereby called ASSIST, leverages the unique way air particles in the atmosphere absorb and emit infrared radiation (Michaud-Belleau et al., 2025). The energy these particles absorb/emit, the spectra, changes with the surrounding thermodynamic conditions. The ASSIST observes the spectral radiance at the surface and the cloud base height, while the TROPoe algorithm, or Tropospheric Remotely Observed Profiling via Optimal Estimation, estimates temperature profiles by inversely solving the radiative transfer equation

$$B(\tilde{v}) = a_{\tilde{v}} \int_{0}^{\infty} B_0(\tilde{v}, T(z)) e^{-a_{\tilde{v}} z}\, dz \tag{1}$$

where $B(\tilde{v})$ is the radiance at a given wavenumber $\tilde{v}$, $a_{\tilde{v}}$ is an absorption coefficient, and $B_0(\tilde{v}, T(z))$ represents the sum of spectral radiance along the height as a function of wavenumber and temperature at each height, $T(z)$ (Michaud-Belleau et al., 2025; Letizia et al., 2025). The ASSIST easily captures wavenumber ranges such as $500-750\,cm^{-1}$, $1250-2000\,cm^{-1}$, and $2250-2380\,cm^{-1}$, which absorb more energy near the surface. During overcast events, the ASSIST demonstrates greater uncertainty in capturing any wavenumbers above the cloud base height.

The ASSIST dataset contains profiles of temperature, potential temperature, relative humidity, cloud base height, and many others. The most relevant ASSIST profiles for this study are temperature, pressure, and relative humidity, which are used to calculate the virtual potential temperature. These profiles are measured from the surface height up to 17 kilometers, with height intervals and thicknesses that increase with altitude. starting with the lowest height interval being from the surface to 10 m.

2.5 Sonic anemometer data

In addition to the remote sensing instrumentation, the barge's 25-m observational tower enabled low-flow distortion observations of the predominant southwesterly winds. Sonic anemometers were deployed at five measurement heights (6.64, 8.84, 11.02, 16.1, and 24.0 m, relative to water surface assuming a 1.52 m barge draft) reporting fluctuations of virtual temperature and three components of velocity at 20 Hz (at 24 m) or 32 Hz (all other heights). The sonic anemometer at 24 m, mounted on a 1.22 m boom was a Gill R3-50 sonic anemometer with a Systron Donner MotionPAK (Edson et al., 1998) while the other levels hosted RM Young 81000RE sonic anemometers on 1.55 m booms. All booms were pointed to 210 degrees. Data were removed during times of precipitation as detected by a RM Young precipitation gauge at 14 m on the tower. The barge was moored, resulting in motion less than that of a buoy or ship, but motion correction was applied to the sonic anemometer data. Fluxes were calculated from 20-minute eddy-covariance averages.

2.6 Dataset Regularization

To calculate stability metrics over a given height interval, the static stability and shear effects must be calculated over matching intervals. Because Bulk Richardson number requires wind and thermodynamic measurements on identical vertical grids, the ASSIST profiles were interpolated onto the lidar measurement heights.

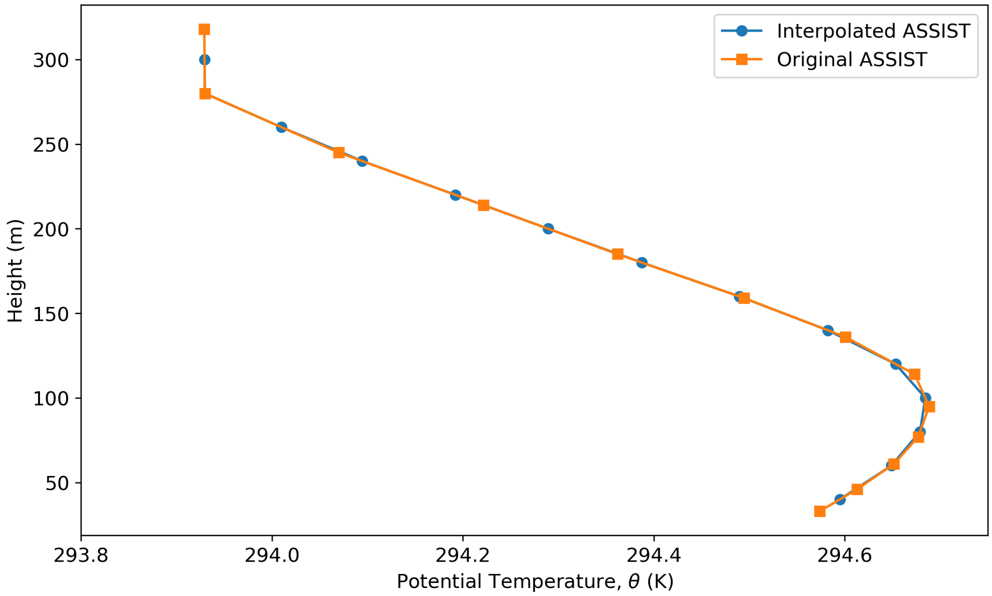

Figure 3. Example of interpolation performed on potential temperature between 40-300 meters

The WindCube V2 provides a uniformly spaced grid of wind profiles between 40 and 300 meters, while the ASSIST spectrometer provides a non-uniform distribution of temperature profiles between 0 and 17 kilometers. To resolve this discrepancy, we linearly interpolated the relevant ASSIST profiles between 33 and 318 meters (the first heights just below and above 40 and 300 meters, respectively) to obtain values every 20 meters in height until 300 meters (Figure 3). This interpolation produced a thermodynamic dataset with uniformly distributed data along the height to match the height resolution of the WindCube.

Furthermore, the WindCube provides 10-minute averages of wind velocity profiles across the summer. The ASSIST also provides 10-minute averages, but offset from the lidar by 5 seconds. This study merely shifted the ASSIST temporal coordinates to remove the offset and ensure compatibility between the two dataset time coordinates. Since the ASSIST only featured a 5 second difference compared to the WindCube, the expected distortion of the temporal data is negligible and allows for direct comparison between the instruments to calculate the Bulk Richardson number.

For comparison of this elevated Bulk Richardson number at 10-minute intervals to the Obukhov Length calculated from the sonic anemometer data at 20-minute intervals, no temporal interpolation was performed. Instead, each 20-min sonic observation was assigned to the two corresponding 10-min bulk Richardson number time stamps.

https://doi.org/10.5194/wes-2026-115
Preprint. Discussion started: 8 July 2026

2.7 Dataset Availability

2.7.1 Lidar and ASSIST data

Neglecting null values and off-station dates (Table 1), the lidar and ASSIST datasets demonstrated a total data return of 62.1% and 79.4%, respectively, after removing any unavailable data between both instruments at the 40 m - 60 m and 120 m - 160 m height intervals. The static stability and Bulk Richardson number were only calculated when both datasets contained values at the same heights and times. If one dataset did not include a value at a particular height and/or time, then the stability metrics were not calculated.

2.7.2 Meteorological Tower Data

Each of the tower sonic anemometers functioned differently during the deployment, with variable data return rates. The data availability rates for each level are shown in Figure 2. Only the 6.64 m and the 24.0 m sonic anemometer functioned for most of the on-station time periods, so either of them can provide the required measurements of the horizontal and vertical components of the flow as well as sonic temperature. Both the 6.64 m and 24 m sonic provided data in excess of 97% of the time the barge was on-station.

3 Methods

The objective of this study is to determine how frequently atmospheric stability inferred from surface observations differs from the stability experienced within the turbine rotor layer. To accomplish this, we compare two complementary stability metrics. Surface-layer stability is characterized using the Obukhov Length derived from sonic anemometer observations, while rotor-layer stability is characterized using the Bulk Richardson number calculated from co-located wind and thermodynamic profiles. Static stability, based solely on the vertical temperature gradient, is also evaluated to distinguish thermally-driven stability changes from those influenced by vertical wind shear.

3.1 Stability Metrics

3.1.1 Static Stability

Static stability, neglecting mechanical shear effects, is determined from the vertical gradient of virtual potential temperature. The Brunt-Väisälä frequency describes the frequency at which a displaced particle oscillates in a stably stratified atmosphere (Vallis, 2017):

$$N^2 = \frac{g}{\theta_v}(\frac{\partial \theta_v}{\partial z}) \tag{2}$$

where θ_v is the virtual potential temperature. Rather than evaluating N^2 directly, We use the bulk virtual potential temperature gradient ($\frac{\Delta \theta_v}{\Delta z}$) which provides an equivalent classification of static stability over each height interval. Negative values indicate statically unstable conditions and positive values indicate statically stable conditions. Because this metric depends only on the temperature structure of the atmosphere, it neglects the effects of mechanical turbulence generated by wind shear. Data from the 6.64 m and 24 m sonic anemometers are used for the Obukhov Length calculations.

3.1.2 Surface-Layer Dynamic Stability

Surface-layer dynamic stability is quantified using the Obukhov Length determined from surface fluxes of heat and momentum:

$$L = \frac{-\overline{\theta}_v u_*^3}{kg(\overline{w'T_v'})}, \tag{3}$$

where u_* is friction velocity:

$$u_*^2 = (\overline{u'w'}^2 + \overline{v'w'}^2)^{1/2}, \tag{4}$$

k is the von Kármán constant, g is gravitational acceleration, and $\overline{w'T_v'}$ is the kinematic heat flux. To calculate the fluxes, the eddy covariance method applies to the perturbations based on twenty-minute means of the u (streamwise), v (transverse), and w (vertical) components of wind speed and the virtual temperature T_v. Here, T_v is taken as the sonic anemometer temperature (Burns et al., 2012). Surface stability is evaluated independently using both the 6.64 m and 24 m sonic anemometers to examine the sensitivity of the results to measurement height. Because the sonic-temperature approximation neglects small humidity-related differences between sonic and virtual temperature, we tested the sensitivity of the stability classification using latent heat flux measurements to estimate a humidity correction to the buoyancy flux. This correction changed the sign of the buoyancy flux, and therefore the sign of L, for only 1.04% of observations at 6.64 m and 1.34% of observations at 24 m. Thus, while the correction may affect the magnitude of L, it does not materially affect the stable/unstable classifications or the reported decoupling statistics.

The Obukhov Length combines the competing influences of buoyancy and mechanical shear on turbulence generation within the atmospheric surface layer. Throughout this study, $L < 0$ m denotes unstable surface conditions, while $L > 0$ m denotes stable surface conditions. We note that it is possible to incorporate the sign of $(u'w')$ into the definition of L. Positive u_* is the standard treatment because friction velocity is a magnitude of the turbulent stress vector. However, we tested the sensitivity of assigning the sign of $\overline{u'w'}$ to u_*, and the resulting stability classifications changed by only 2.5% at 6.64m and 7.1% at 24 m, indicating that the conclusions are insensitive to this treatment.

3.1.3 Rotor-Layer Dynamic Stability

The Bulk Richardson number compares buoyancy due to thermal gradients and shear produced by convection in the atmosphere (Stull, 1988). The Bulk Richardson number is calculated over a height interval rather than at a discrete point so the competing effects of static stability and shear can be evaluated over a layer instead of at a point:

$$Ri_B = \frac{g\Delta\theta_v\Delta z}{\overline{\theta_v}(\Delta U^2 + \Delta V^2)} \tag{5}$$

where θ_v is the virtual potential temperature, U is the zonal (east-west) velocity and V is the meridional (north-south) wind component.

Unlike the Obukhov Length, which characterizes turbulence based on data at a single observation height, the Bulk Richardson number evaluates the balance between buoyancy and vertical wind shear across an entire layer. It is therefore well suited for describing atmospheric stability throughout the turbine rotor disk.

Bulk Richardson numbers are calculated over two layers:

- 40–60 m, representing the lowest altitude interval available from the collocated remote sensing instruments, and
- 120–160 m, representing the hub-height region of modern offshore wind turbines.

The primary analysis focuses on the 120–160 m layer because it most directly characterizes the atmospheric conditions experienced by utility-scale offshore wind turbines. The lower layer is used to examine how rapidly stability transitions occur between the surface layer and rotor height.

Although critical Richardson numbers near 0.25 are often used to diagnose the onset of turbulence (Stull, 1988), the objective of this study is to distinguish stable and unstable atmospheric regimes rather than identify the precise transition to turbulence. Accordingly, positive Bulk Richardson numbers are classified as stable and negative values as unstable. A sensitivity study to the choice of this threshold appears in the Appendix, supporting the choice of a threshold at 0.

3.2 Coupled and Decoupled Stability

The central question of this study is whether stability inferred from surface observations accurately represents stability within the turbine rotor layer. For every observation period, the surface-layer stability classification obtained from the Obukhov Length is compared with the corresponding Bulk Richardson number classification within the rotor layer. Four possible combinations exist:

- Coupled Stable: both surface layer and rotor layer stable
- Coupled Unstable: both surface layer and rotor layer unstable
- Decoupled, surface unstable: surface-unstable/ rotor-stable
- Decoupled, surface stable: surface-stable/ rotor-unstable.

The primary focus of this paper is the surface-unstable / rotor-stable decoupling regime. During these periods, conventional surface measurements indicate unstable atmospheric conditions while the turbine rotor layer remains stably stratified. Relying solely on surface observations under these conditions may therefore underestimate atmospheric stability relevant to wind turbine wakes, power production, and structural loading.

https://doi.org/10.5194/wes-2026-115
Preprint. Discussion started: 8 July 2026

3.3 Event identification

To quantify both the occurrence and persistence of stability decoupling, consecutive observations classified as surface-unstable / rotor-stable are grouped into individual decoupling events. Events separated by one or more observations that do not satisfy the decoupling criterion are treated as distinct episodes. For each event, we calculate the start time, end time, duration, median Obukhov Length, median Bulk Richardson number, and maximum Bulk Richardson number.

Throughout the remainder of this paper, comparisons between surface and rotor-layer stability refer to the 24 m Obukhov Length and the 120–160 m Bulk Richardson number unless otherwise stated. Results are very similar between the two layers and the 24-m level is selected to avoid any question of flow distortion from the barge itself.

4 Results

4.1 Meteorological Overview of Summer 2024

Summer winds were predominantly southwesterly (Figure 4a), consistent with other observations conducted in this region during the summer (Bodini et al., 2019; Debnath et al., 2021) as well as modeling studies (Quint et al., 2025). The infrequent northeasterly winds feature slower speeds than the southwesterly winds. Most wind speeds fall between 7.5-9.5 m s^{-1} at the lowest lidar level (40 m), and even faster at the hub-level 140 m, peaking around 18 m s^{-1} (Figure 5).

The diurnal cycle over water differs substantially from that over land because of the large heat capacity of the ocean (Shaw et al., 2022). The median air temperatures measured at 7.87 and 23.3 m exhibit a weak diurnal cycle, with minimum temperatures occurring shortly after sunrise (08:00–09:00 ET; 12:00–13:00 UTC) and maximum temperatures occurring during the late afternoon and evening (16:00–18:00 ET; 20:00–22:00 UTC) (Figure 6a). The temperature evolution is nearly identical at both levels, with median differences generally less than 0.3°C throughout the day, indicating weak mean thermal variability within the lowest 25 m.

Despite these small mean temperature differences, the turbulent heat flux exhibits a clear diurnal cycle near the surface (Figure 6b). At 6.64 m, the median heat flux becomes positive shortly after sunrise, remains upward throughout the daytime, and returns toward zero after sunset, consistent with solar warming of the ocean surface and the resulting destabilization of the lowest portion of the atmospheric boundary layer. In contrast, the median 24 m heat flux remains weakly negative or near zero throughout the diurnal cycle. While the median 24 m flux is slightly negative during many hours, its magnitude is small relative to the variability shown by the interquartile range (Figure 6b). Therefore, rather than indicating persistent downward heat transport, the 24 m observations suggest that the surface-driven diurnal heating signal evident at 6.64 m is attenuated by 24 m. The differing behavior of the two flux levels, despite nearly identical mean temperatures, provides an early indication that the coupling between the ocean surface and the lower rotor layer is often weak or not present.

Surface heating generates weak daytime destabilization near the ocean surface (Figure 6), yet this destabilization rarely extends through the rotor layer, where the median virtual potential temperature gradient remains positive throughout the day (Figure 7a). According to the ASSIST measurements, the average change in potential temperature over height is positive from

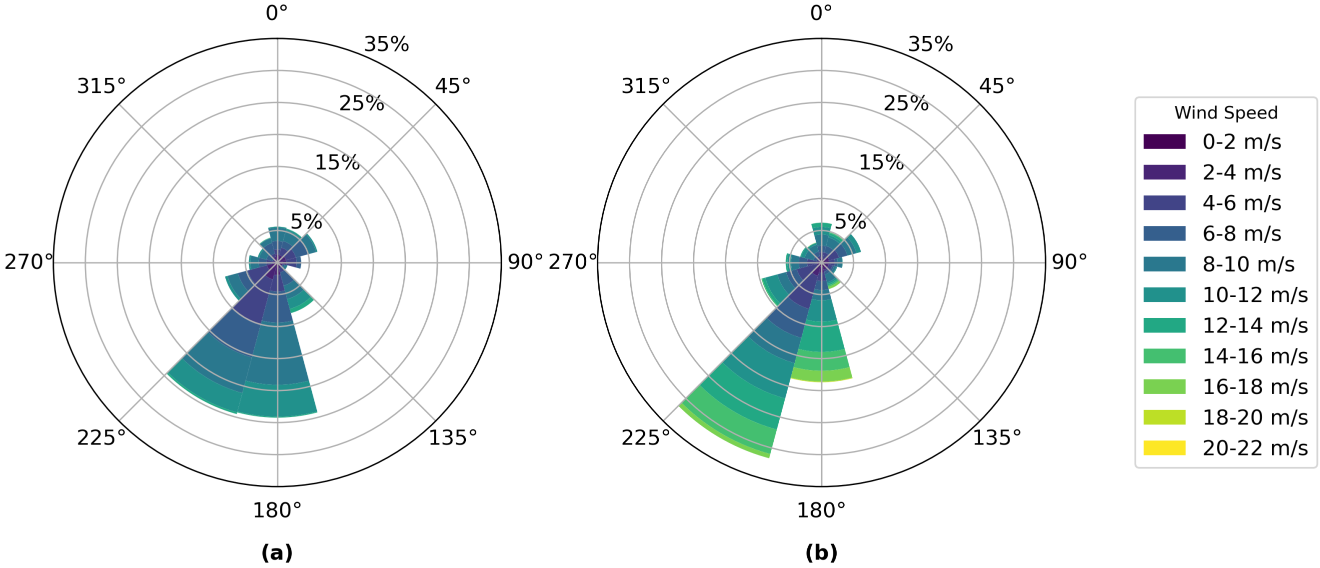

Figure 4. Wind roses for the entire summer where data was available and on-station. **(a)** shows the wind at 40 m, the lowest lidar level, and **(b)** shows the wind at 140 m, representing hub-level.

40 - 60 m and 120 m - 160 m, indicating largely stable conditions throughout the summer (Figure 7). Nonetheless, the change in potential temperature over the lower layer (40-60 m) (Figure 7b)has a wider distribution that dips into negative changes, indicating more tendency towards unstable conditions throughout the day closer to the surface than throughout the hub-layer (120-160 m) (Figure 7a). These excursions into unstable conditions tend to occur during the day, between 14:00-21:00 UTC (10:00-17:00 ET).

4.2 Decoupling between the surface and rotor region assessed

Surface-rotor stability decoupling occurs in nearly one third of the observed times regardless of the stability metrics used. In Figure 8 we compare sonic-derived Obukhov Length with the bulk Richardson number calculated over the 120–160 m layer. Each point represents a matched 10-minute observation, classified according to whether the surface layer (determined by the sonic anemometer) and rotor layer (determined by the ASSIST and profiling lidar) are stable or unstable. Agreement between the two stability measures occurs when both indicate stable conditions (upper right quadrant, blue) or both indicate unstable conditions (lower left quadrant, red). Of greater interest are the off-diagonal quadrants, which represent vertical decoupling between the surface and rotor layer. In particular, the upper left quadrant (purple) identifies periods in which the surface layer is convectively unstable while the rotor layer remains stably stratified. Such conditions imply that turbulence generated near the surface is confined to a shallow layer and does not extend through the turbine rotor, challenging the common assumption that near-surface measurements provide a representative estimate of the stability experienced by offshore wind turbines.

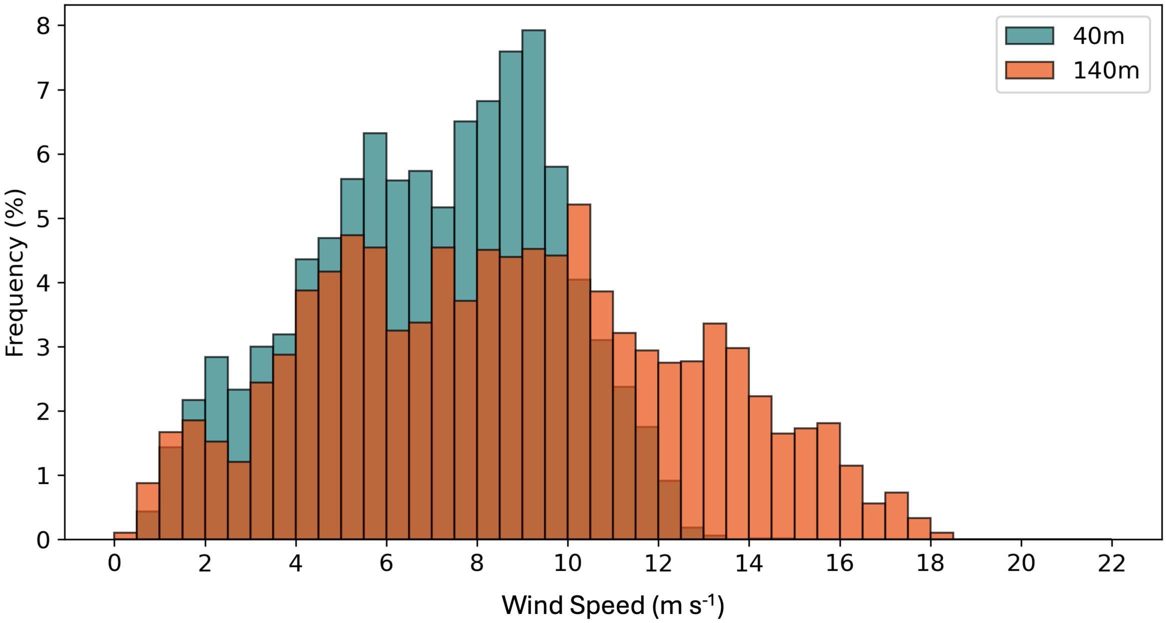

Figure 5. Wind speed distributions for the entire summer when data was available and the barge was on-station.

The dominant feature of Figure 8 is the frequent occurrence of this decoupled regime. Using the 6.64 m sonic, 37.6% of all matched observations exhibit unstable surface conditions beneath a stably stratified rotor layer, compared with 51.4% that are stably stratified throughout the profile. Even when the surface stability estimate is moved upward to 24 m, the decoupled regime remains remarkably common, accounting for 30.6% of all observations (95% confidence interval based on 1000 resampled datasets: 28.3–30.7%). In contrast, the opposite configuration, a stable surface layer beneath an unstable rotor layer, is rare (<4%, 95% confidence interval: 3.0–3.9%)). The non-overlapping confidence intervals indicate that the strong asymmetry between the two forms of decoupling is robust and unlikely to arise from sampling variability alone.

To ensure these statistics are not artifacts of near-neutral conditions, we removed near-neutral conditions, requiring that the absolute values of both the Obukhov Length $|L| > 50$ m and the Bulk Richardson number $|Ri| > 0.05$. The distribution of data points persists with 29.5 % of data points surface-unstable/rotor-stable and 3.1 % surface-stable/rotor-unstable (instead of 30.6 % surface-unstable/rotor-stable and 3.6 % surface-stable/rotor-unstable for all data).

The disagreement between surface-layer and rotor-layer stability classifications is strongly asymmetric. Stable rotor-layer conditions frequently coexist with unstable surface conditions, whereas the reverse configuration is rare. This asymmetry persists after excluding near-neutral observations, indicating that the result is not simply a consequence of threshold sensitivity near neutral stability. This distribution suggests a persistent tendency for convective mixing to remain confined to the lowest tens of meters while the rotor layer remains stably stratified. Thus, at this offshore location, nearly one out of every three available observations would incorrectly classify rotor-layer stability if only surface observations were available.

https://doi.org/10.5194/wes-2026-115
Preprint. Discussion started: 8 July 2026

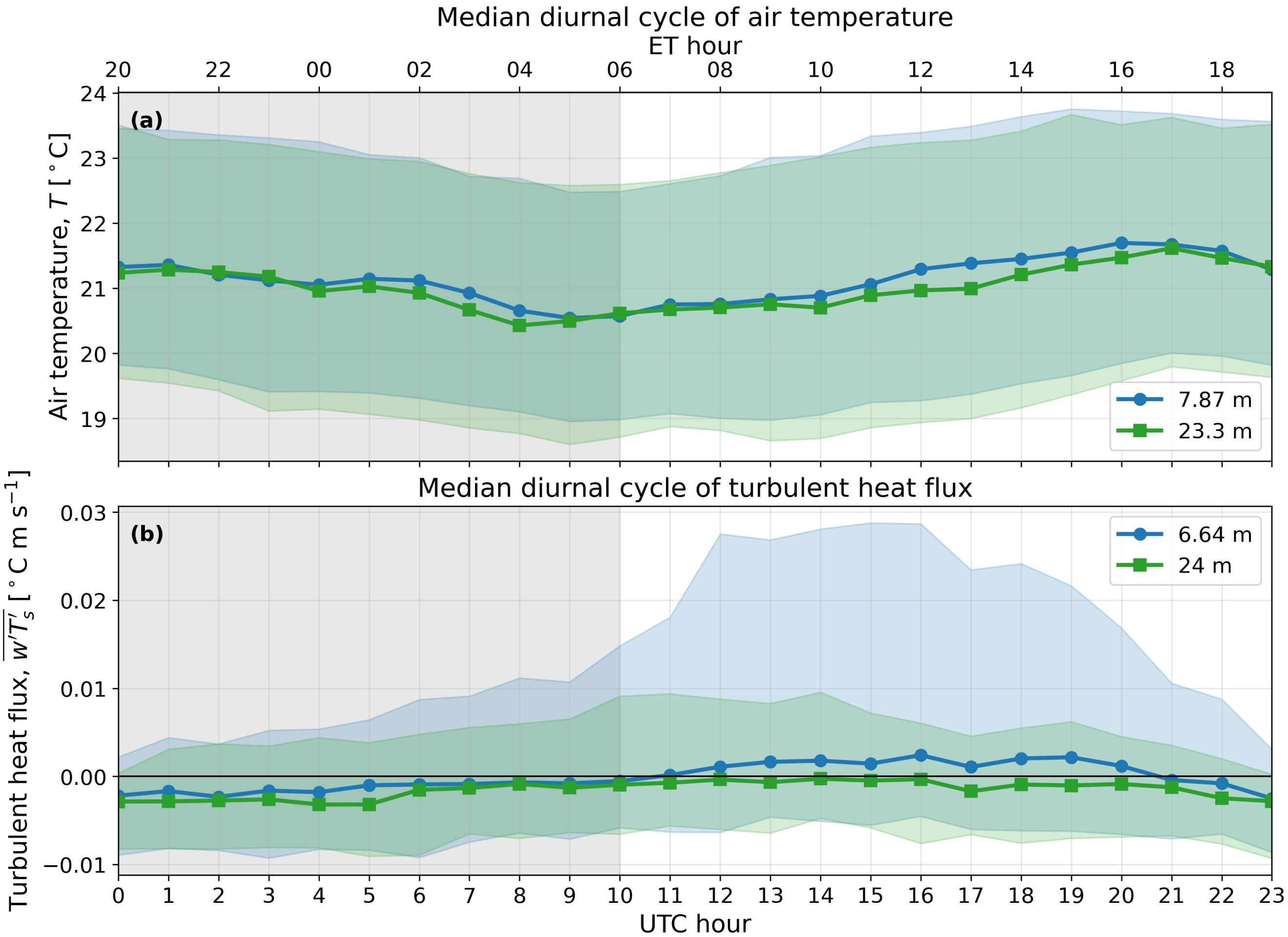

Figure 6. Diurnal cycles of (a) hourly median virtual temperature (sonic temperature) and (b) hourly median heat flux when data was available and on-station. Shading indicates the interquartile range across all valid on-station observations in each UTC hour; asymmetry reflects the skewed distribution of turbulent heat fluxes rather than a symmetric uncertainty estimate. The gray shaded background represents nighttime. Bottom axis shows UTC; top axis shows Eastern Time (ET).

https://doi.org/10.5194/wes-2026-115
Preprint. Discussion started: 8 July 2026

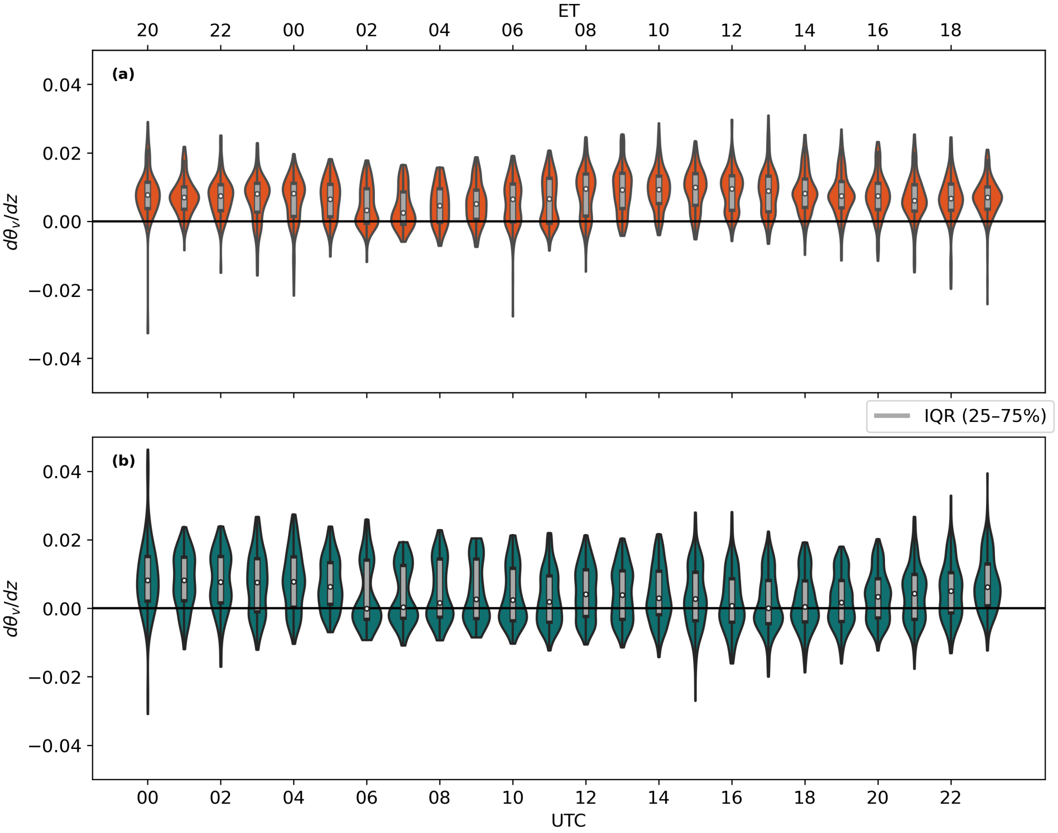

Figure 7. Distribution of the virtual potential temperature gradient, $\partial\theta_v/\partial z$ (°C m^{-1}), as a function of UTC hour for the 120–160 m layer **(a)** and the 40–60 m layer **(b)**. Each violin represents the full distribution of all 10-minute observations within a given hour of the day, where the width of the violin is proportional to the probability density of the observations. The embedded gray box denotes the interquartile range (25th–75th percentiles), the horizontal line within the box indicates the median, the white circle marks the mean, and the thin black line shows the full range of the data. Positive values correspond to statically stable stratification, while negative values indicate unstable stratification. Bottom axis shows UTC; top axis shows Eastern Time (ET).

https://doi.org/10.5194/wes-2026-115
Preprint. Discussion started: 8 July 2026

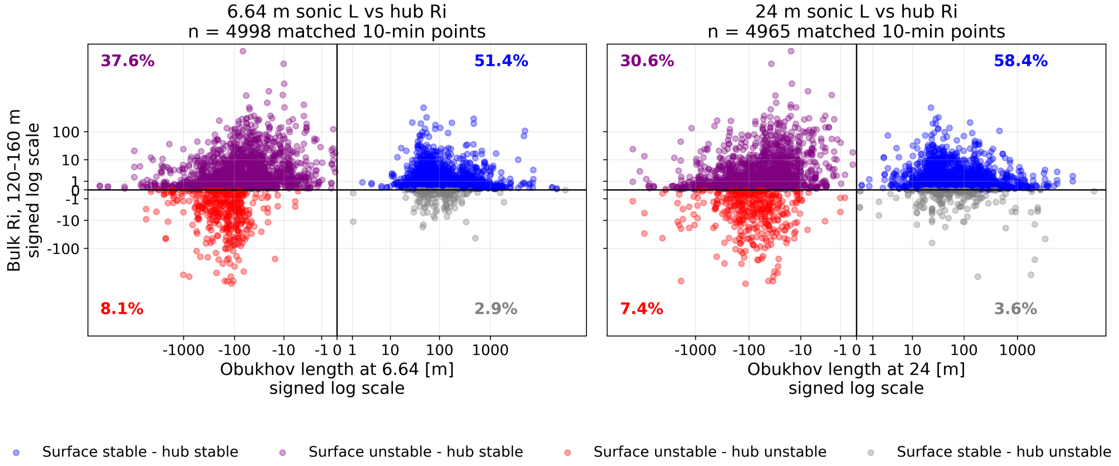

Figure 8. Comparison of surface-layer stability using Obukhov Length from (a) 6.64 m and (b) 24 m compared to bulk Richardson number over 120 m - 160 m altitude. Top right (blue) quadrants indicate coupled stable, bottom left (red) quadrants indicate coupled unstable, top left (purple) quadrants indicate surface-unstable/rotor-stable, bottom right (gray) indicates surface-stable/rotor-unstable. Data include the entire on-station summer. Axes use a signed logarithmic transform, $sign(x)\log(1+\mid x\mid)$, to show both near-neutral and extreme values while preserving the stable/unstable quadrants.

Finally, agreement on the assessment of stability between the 6 m and 24 m Obukhov Length classifications exceeds 88%, indicating that these decoupling results are robust to the choice of level for the surface stability assessment.

4.3 Diurnal and Monthly Variability of Decoupling Events

Seasonal variability of decoupling dominates diurnal variability of decoupling during the limited 4-month deployment of the barge (Figure 9). During June, this decoupled stability state is relatively uncommon, generally occurring in less than 20% of available observations. Frequencies increase during July and become widespread by September, when the decoupled state is observed during approximately 70–90% of available observations. Although modest hour-to-hour variability occurs, particularly during late summer, no single hour consistently dominates the occurrence of decoupling. Instead, once the decoupled regime develops seasonally, it persists throughout much of the diurnal cycle.

Similar behavior is found using the 6.64 m sonic (not shown), with generally more frequent decoupling, indicating that the result is robust to the choice of sonic level.

The seasonal increase in decoupling is not explained by weaker surface buoyancy forcing. Median Obukhov lengths become more negative during much of the daytime throughout late summer (Figure 10), indicating continued surface-driven convective turbulence. In contrast, median Bulk Richardson numbers within the rotor layer increase substantially from June through September (Figure 11), indicating progressively stronger elevated stratification. The increasing separation between surface and rotor-layer stability demonstrates that the seasonal increase in decoupling frequency is driven by interactions between the

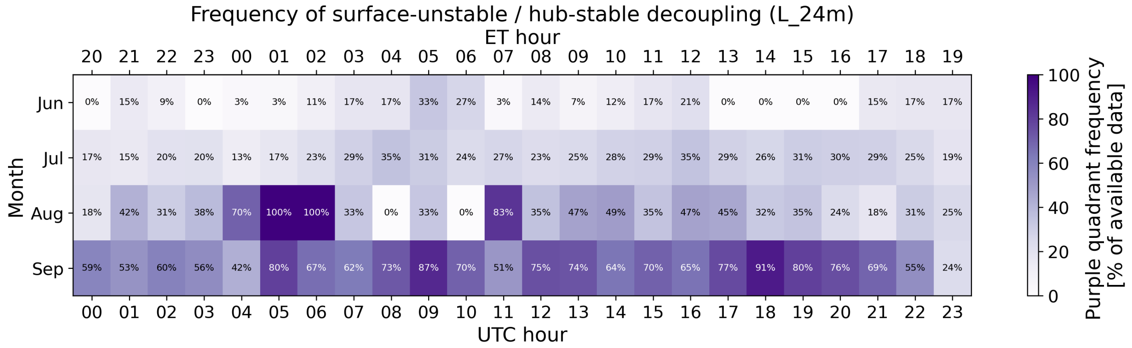

Figure 9. Heat map showing diurnal and monthly frequency of decoupling events defined by 24-m Obukhov Length vs. 120-160 m Richardson number. Bottom axis shows UTC; top axis shows Eastern Time (ET).

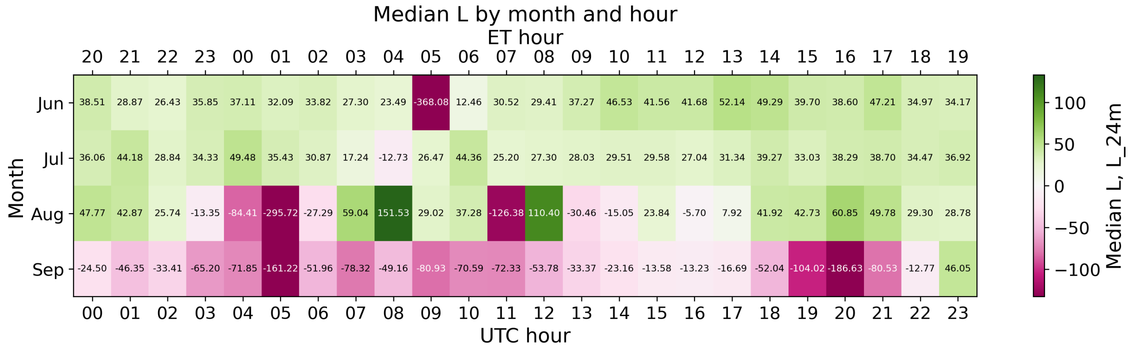

Figure 10. Heat map showing diurnal and monthly median 24-m Obukhov Length. Bottom axis shows UTC; top axis shows Eastern Time (ET).

strengthening stratification aloft and changes in the surface energy balance. As summer transitions to fall, the marine boundary layer transitions to a shallow surface mixed layer beneath a persistent stable rotor layer.

4.4 Frequency and Duration of Decoupling Events

Comparing the frequency and duration of these decoupling events by month reveals that the character of the decoupling changes through the summer (Figure 12). Although decoupling becomes more frequent during September (even accounting for the increased data availability in September), the individual episodes become shorter-lived. This shift reflects the progressive strengthening of hub-height stratification throughout the summer. July and August include fewer but more persistent decoupling episodes, whereas September is characterized by a background state that is frequently favorable for decoupling but more temporally intermittent. The median L and Bulk Richardson heat maps together suggest that this shift is not caused by weak-

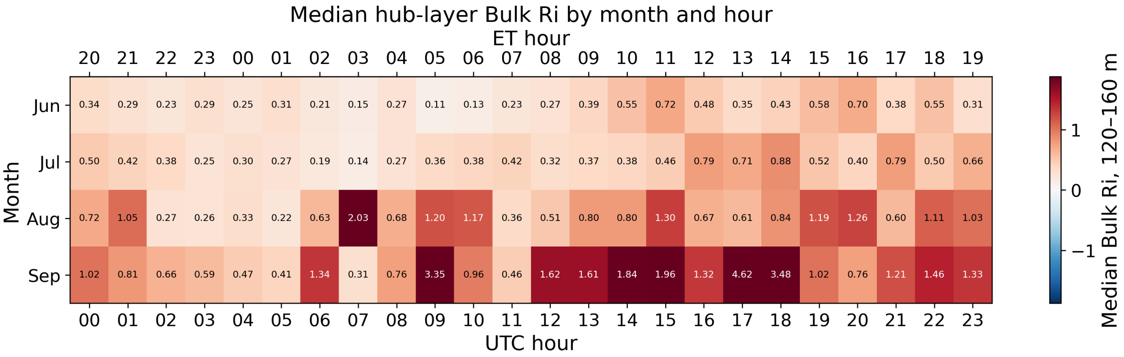

Figure 11. Heat map showing median 120-160 m Richardson number. Bottom axis shows UTC; top axis shows Eastern Time (ET).

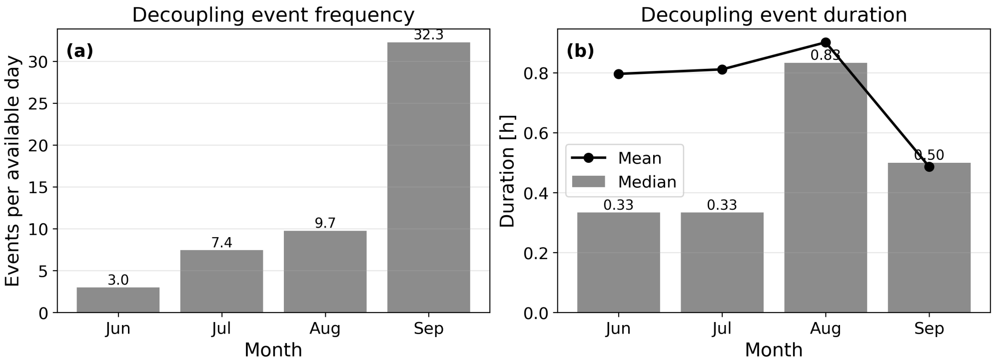

Figure 12. Evaluation of decoupling events by month, (a) Frequency of events per available data, (b) Mean and median duration of available events.

ened surface instability; rather, it reflects increasingly stable rotor-layer stratification superimposed on variable surface-layer forcing.

325 4.5 Distribution of Winds during Decoupling Events

Unstable-surface/stable-hub conditions feature slower wind speeds than all other stability conditions (Figure 13), with an average wind speed around 6.11 $\mathrm{ms^{-1}}$ and a maximum speed of 17.42 $\mathrm{ms^{-1}}$. Meanwhile, coupled-stable conditions feature the fastest wind speeds, averaging 9.84 $\mathrm{ms^{-1}}$ and reaching a maximum of 21.72 $\mathrm{ms^{-1}}$. Faster wind speeds are correlated to more stable rotor layer conditions, suggesting that convective mixing may encourage temperature homogenization. The preferential occurrence of decoupling during slower wind speeds does not arise from a particular wind direction, as decoupled cases are observed across the prevailing southwesterly flow as well as less frequent northeasterly winds (not shown).

https://doi.org/10.5194/wes-2026-115
Preprint. Discussion started: 8 July 2026

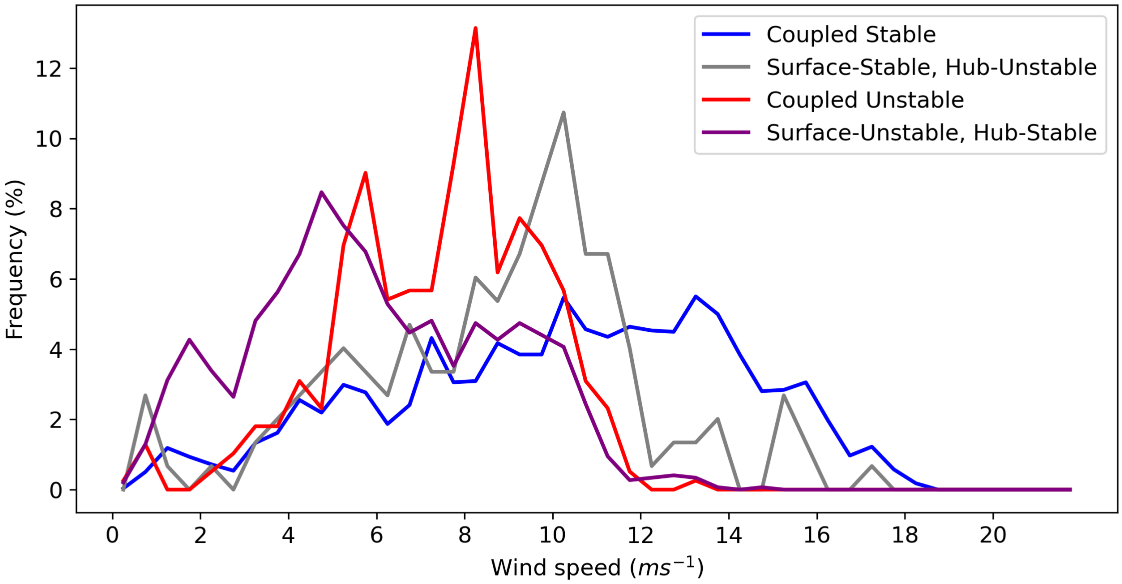

Figure 13. Hub-height (140 m) wind speed distributions pertaining to each quadrant in Figure 8.

5 Conclusions

Atmospheric stability is commonly inferred from measurements made near the ocean surface, yet offshore wind turbines operate within a rotor layer extending more than 100 m above the sea surface. Using collocated sonic anemometer, profiling lidar, and thermodynamic profiler observations collected during the WFIP3 barge deployment in the summer of 2024, we quantify how frequently conventional surface-based stability estimates represent the atmospheric stability experienced within the turbine rotor layer.

Surface observations often fail to represent rotor-layer stability. Approximately one-third of all matched observations exhibit unstable conditions near the surface while the 120-160 m rotor layer remains stably stratified. In contrast, the opposite configuration, a stable surface layer beneath an unstable rotor layer, occurs only rarely. These results demonstrate that the dominant form of stability decoupling over the summer marine boundary layer off the U.S. East Coast is a shallow unstable surface layer underlying a persistently stable rotor layer. Consequently, atmospheric stability inferred solely from near-surface observations would misclassify the stability experienced by offshore wind turbines during a substantial fraction of summertime conditions.

The occurrence of decoupling increases markedly throughout the summer, rising from relatively infrequent events during June to the dominant stability regime during September. This seasonal evolution is not accompanied by an equally strong diurnal cycle, suggesting that background marine stratification exerts a stronger control on decoupling than the daily surface energy balance. As hub-height stability strengthens through late summer, relatively weak daytime surface heating generates only shallow convective mixing that remains confined below the turbine rotor layer. Although decoupling becomes more frequent during September, individual events become shorter-lived, indicating that the atmosphere transitions repeatedly between coupled and decoupled states once the rotor layer approaches persistent stable stratification.

These findings have important implications for offshore wind energy observations. Many observational studies, operational monitoring systems, and floating lidar deployments characterize atmospheric stability using measurements made near the sea surface, in some cases relying on the temperature difference between the air and water to approximate stability. Our results demonstrate that surface-based measurements cannot be assumed to represent the atmospheric conditions experienced throughout the turbine rotor layer, particularly during summer marine conditions. As offshore wind turbines continue to increase in hub height and rotor diameter, the vertical separation between conventional surface observations and the region of turbine operation will continue to grow, making representative stability measurements increasingly important.

The results also have implications for evaluating atmospheric models. Agreement between modeled and observed surface stability does not necessarily imply that the model accurately reproduces the stability structure throughout the turbine rotor layer. Future evaluations of mesoscale numerical weather prediction models and large-eddy simulations should therefore assess vertically resolved stability whenever profile observations are available. Likewise, studies investigating wind-farm wakes, wake steering, turbine loading, and power production should consider whether stability classifications derived from surface observations accurately represent rotor-height conditions.

Previous studies have identified the occurrence of shallow unstable layers beneath more stable conditions aloft in offshore environments in both observations (Platis et al., 2022; Cimini et al., 2025) and mesoscale simulations (Rosencrans et al., 2024; Xia et al., 2025). Building on those contributions, this study quantifies the frequency, persistence, and seasonal evolution of these decoupled stability regimes using co-located turbulence, wind-profile, and thermodynamic measurements. Framing the analysis in terms of the representativeness of conventional surface observations provides a practical perspective for offshore wind resource assessment, atmospheric model evaluation, and wind-farm applications.

Several important questions remain. The present analysis is limited to a single summer deployment off the northeastern United States, and similar analyses are needed during other seasons and in other offshore environments to determine the generality of these findings. Future work should also investigate the meteorological conditions associated with decoupling, including cloud cover, precipitation, and synoptic forcing, as well as evaluate whether current mesoscale and large-eddy simulations reproduce the observed frequency, duration, and seasonal evolution of decoupled stability regimes. Improving our understanding of when and why the marine boundary layer becomes vertically decoupled will ultimately lead to more representative offshore observations, more rigorous atmospheric model evaluation, and more accurate prediction of offshore wind turbine performance.

Code and data availability. The relevant datasets can be found at https://doi.org/10.21947/2569229 (Letizia, 2025), https://doi.org/10.21947/2569228 (Bodini, 2025), and https://doi.org/10.21947/2476341 (Zippel, 2026). The code used to process the data sets is available at https://github.com/valeria-vasquez-barros/BargeStabilityDecoupling (Vasquez-Barros, 2026).

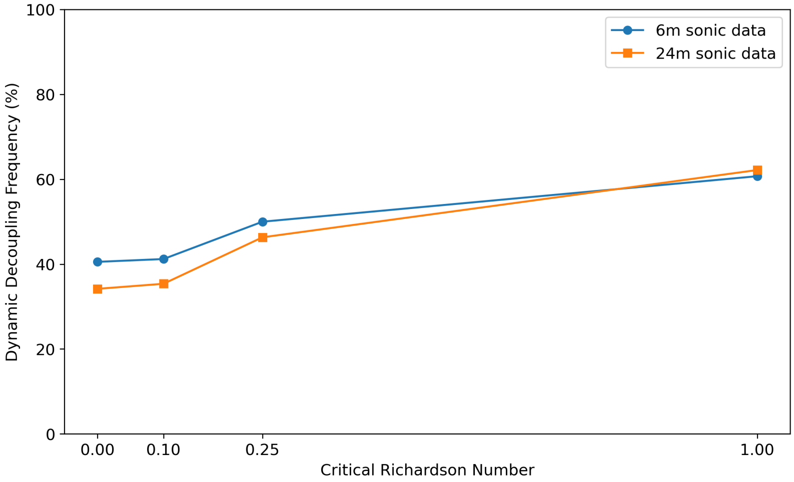

Figure A1. Dynamic decoupling frequency as a function of the critical Richardson number

Appendix A: Sensitivity of Critical Richardson Number

We conducted a sensitivity analysis using the Bulk Richardson values from this analysis to determine the most suitable critical Richardson number (Figure A1). A critical Richardson number of 0 demonstrates the most conservative and realistic cutoff for turbulence and stable conditions. Thus, when $Ri_B > 0$, we define the target atmospheric region as dynamically stable, and when $Ri_B < 0$, the target atmospheric region is considered dynamically unstable.

Author contributions. VVB acquired funding and carried out the formal analysis and investigation, including software development, visualization, and writing the initial draft. JKL was responsible for the conceptualization and supervision of the project, and carried out some formal analysis and investigation, including software development and visualization. NB was also responsible for the conceptualization. SZ carried out the sonic anemometer eddy covariance calculations. AK designed, led, and managed the Barge deployment. All authors reviewed and edited the publication.

Competing interests. At least one co-author is a member of the WES Editorial Board.

Acknowledgements. The authors express great appreciation to the WFIP Barge design and deployment team at WHOI, particularly Eve Cinquino, as well as to Raghu Krishnamurthy for providing the motion-corrected lidar dataset. We thank Andrew Scholbrock and Dave Jager for helping with the deployment of the lidar and ASSIST on the WFIP3 barge, and Stefano Letizia for curating the ASSIST observations. VVB thanks Nathan Agarwal, Amelia Adcroft, and Martin Beshara for their guidance throughout the analysis and writing process. We also express appreciation to Prof. Charles Meneveau for internal review of this manuscript. Finally, we thank the Ralph O'Connor Sustainable Energy Institute and Academic Center for Reliability and Resilience of Offshore Wind for their support in this project. This material is based in part by work initially supported by the U.S. Department of Energy's Office of Energy Efficiency and Renewable Energy (EERE) under the Wind Energy Technologies Office (WETO) Award Number DE-EE0011269, and continuing support from the Massachusetts Clean Energy Center and the Maryland Energy Administration. The views expressed herein do not necessarily represent the views of the U.S. Department of Energy, the United States Government, the Massachusetts Clean Energy Center or the Maryland Energy Administration. The authors used OpenAI's ChatGPT to assist with developing Python code for data processing and visualization. All scientific analyses, interpretation of results, and final manuscript content were independently reviewed and approved by the authors, who assume full responsibility for the work.

References

Adler, B., Bianco, L., Turner, D. D., Olson, J. B., Sun, X., Gebauer, J., Bodini, N., Letizia, S., and Wilczak, J. M.: Multi-season evaluation of temperature and wind in the marine boundary layer along the United States northeast coast in the High-Resolution Rapid Refresh model, https://doi.org/10.5194/egusphere-2026-97, 2026.

Bodini, N.: Lidar / Standardized Data, https://doi.org/10.21947/2569228, 2025.

Bodini, N., Lundquist, J. K., and Kirincich, A.: U.S. East Coast Lidar Measurements Show Offshore Wind Turbines Will Encounter Very Low Atmospheric Turbulence, Geophysical Research Letters, 46, 5582–5591, https://doi.org/10.1029/2019GL082636, 2019.

Bodini, N., Letizia, S., Adler, B., Turner, D. D., Krishnamurthy, R., Scholbrock, A., Jager, D., Cinquino, E., and Kirincich, A.: Observations of offshore low-level jets off the U.S. East Coast reveal systematic biases in ERA5 and HRRR, Geophysical Research Letters, accepted, 2026a.

Bodini, N., Olson, J., Gaudet, B., Iungo, G. V., Shams Solari, M., Roy, S., Lundquist, J. K., Agarwal, N., Myers, T. A., Adler, B., Mirocha, J. D., James, E., Bianco, L., Wilczak, J. M., and Turner, D. D.: A total of 19 months of daily weather logging on the US east coast: the WFIP3 event log, Wind Energy Science, 11, 1949–1961, https://doi.org/10.5194/wes-11-1949-2026, 2026b.

Burns, S. P., Horst, T. W., Jacobsen, L., Blanken, P. D., and Monson, R. K.: Using sonic anemometer temperature to measure sensible heat flux in strong winds, Atmos. Meas. Tech., 5, 2095–2111, https://doi.org/10.5194/amt-5-2095-2012, 2012.

Cimini, D., Gandoin, R., Fiedler, S., Acquistapace, C., Balotti, A., Gentile, S., Geraldi, E., Knist, C., Martinet, P., Nilo, S. T., Pace, G., Pospichal, B., and Romano, F.: Atmospheric stability from numerical weather prediction models and microwave radiometer observations for onshore and offshore wind energy applications, Atmospheric Measurement Techniques, 18, 2041–2067, https://doi.org/10.5194/amt-18-2041-2025, 2025.

Cinquino, E. and Kirincich, A.: WHOI MetOcean Data Initiative, Technical Report WHOI_MetOcean_2024, Woods Hole Oceanographic Institution, https://doi.org/10.26025/1912/27014, 2024.

Debnath, M., Doubrawa, P., Optis, M., Hawbecker, P., and Bodini, N.: Extreme wind shear events in US offshore wind energy areas and the role of induced stratification, Wind Energy Science, 6, 1043–1059, https://doi.org/10.5194/wes-6-1043-2021, 2021.

Djath, B., Schulz-Stellenfleth, J., and Cañadillas, B.: Impact of atmospheric stability on X-band and C-band synthetic aperture radar imagery of offshore windpark wakes, Journal of Renewable and Sustainable Energy, 10, 043 301, https://doi.org/10.1063/1.5020437, 2018.

Edson, J. B., Hinton, A. A., Prada, K. E., Hare, J. E., and Fairall, C. W.: Direct Covariance Flux Estimates from Mobile Platforms at Sea*, Journal of Atmospheric and Oceanic Technology, 15, 547–562, https://doi.org/10.1175/1520-0426(1998)015<0547:DCFEFM>2.0.CO;2, 1998.

Edson, J. B., Crawford, T., Crescenti, J., Farrar, T., Frew, N., Gerbi, G., Helmis, C., Hristov, T., Khelif, D., Jessup, A., Jonsson, H., Li, M., Mahrt, L., McGillis, W., Plueddemann, A., Shen, L., Skyllingstad, E., Stanton, T., Sullivan, P., Sun, J., Trowbridge, J., Vickers, D., Wang, S., Wang, Q., Weller, R., Wilkin, J., Yu, D., and Zappa, C.: The Coupled boundary layers and air-sea transfer experiment in low winds, Bulletin of the American Meteorological Society, 88, 341–356, 2007.

Fleming, P., Annoni, J., Scholbrock, A., Quon, E., Dana, S., Schreck, S., Raach, S., Haizmann, F., and Schlipf, D.: Full-Scale Field Test of Wake Steering, Journal of Physics: Conference Series, 854, 012 013, https://doi.org/10.1088/1742-6596/854/1/012013, 2017.

Keck, R.-E., de Maré, M., Churchfield, M. J., Lee, S., Larsen, G., and Aagaard Madsen, H.: On atmospheric stability in the dynamic wake meandering model, Wind Energy, 17, 1689–1710, https://doi.org/10.1002/we.1662, _eprint: https://onlinelibrary.wiley.com/doi/pdf/10.1002/we.1662, 2014.

Kirincich, A., Krishnamurthy, R., Turner, D., Adler, B., Agarwal, N., Berg, L. K., Bianco, L., Bodini, N., Chabert d'Hieres, M., Farrar, J. T., Fernando, H., Gaudet, B., Ghate, V. P., Goldberger, L., Gonzalez, A. O., Hall, E., Hines, E., Hodges, G., Iungo, G. V., Jackson, R. Jiang, H., Kinsella, A., Kosovic, B., Kotamarthi, R., Letizia, S., Lipari, S., Lundquist, J. K., Mirocha, J., Moss, C., Muradyan, P., Myers, T., Newsom, R., O'Brien, J., Olson, J., Pekour, M., Puccioni, M., Rosencrans, D., Roy, S., Sauvage, C., Sedlar, J., Seo, H., Shams Solari, M., Soldo, L., Stierle, S., Sun, X., Thompson, E., Traiger, E., Wharton, S., Wilczak, J., and Zippel, S.: Improving the Understanding and Forecasting of Winds over the Northeast U.S. Shelf: The Third Wind Forecast Improvement Project (WFIP3), Bulletin of the American Meteorological Society, In Review, 2026.

Krishnamurthy, R., García Medina, G., Gaudet, B., Gustafson, Jr., W. I., Kassianov, E. I., Liu, J., Newsom, R. K., Sheridan, L. M., and Mahon, A. M.: Year-long buoy-based observations of the air–sea transition zone off the US west coast, Earth System Science Data, 15, 5667–5699, https://doi.org/10.5194/essd-15-5667-2023, 2023.

Letizia, S.: NREL ASSIST Barge / Thermodynamic retrievals TROPoe v0.19, https://doi.org/10.21947/2569229, 2025.

Letizia, S., Michaud-Belleau, V., Turner, D. D., and Abraham, A.: Thermodynamic Profiling Through ASSIST Observations and TROPoe Retrievals, Tech. Rep. NREL/TP-5000-92509, National Renewable Energy Lab., Golden, CO (United States), https://docs.nlr.gov/docs/fy26osti/92509.pdf, 2025.

Lundquist, J. K., Churchfield, M. J., Lee, S., and Clifton, A.: Quantifying error of lidar and sodar Doppler beam swinging measurements of wind turbine wakes using computational fluid dynamics, Atmospheric Measurement Techniques, 8, 907–920, https://doi.org/10.5194/amt-8-907-2015, 2015.

Lundquist, J. K., DuVivier, K. K., Kaffine, D., and Tomaszewski, J. M.: Costs and consequences of wind turbine wake effects arising from uncoordinated wind energy development, Nature Energy, 4, 26–34, https://doi.org/10.1038/s41560-018-0281-2, 2018.

Machefaux, E., Larsen, G. C., Koblitz, T., Troldborg, N., Kelly, M. C., Chougule, A., Hansen, K. S., and Rodrigo, J. S.: An experimental and numerical study of the atmospheric stability impact on wind turbine wakes: Experimental and numerical study of the atmospheric stability impact on wake, Wind Energy, 19, 1785–1805, https://doi.org/10.1002/we.1950, 2016.

Michaud-Belleau, V., Gaudreau, M., Lacoursière, J., Boisvert, , Ravelomanantsoa, L., Turner, D. D., and Rochette, L.: The Atmospheric Sounder Spectrometer by Infrared Spectral Technology (ASSIST): instrument design and signal processing, Atmospheric Measurement Techniques, 18, 3585–3609, https://doi.org/10.5194/amt-18-3585-2025, 2025.

Newsom, R. K., Gibler, G., Gaustad, K., and Zhang, D.: Doppler Lidar Motion-Correction (DLMC) Value-Added Product Report, Tech. Rep. DOE/SC-ARM-TR-296, U.S. Department of Energy, Atmospheric Radiation Measurement user facility, Richland, Washington, https://doi.org/10.2172/2318487, 2024.

Olson, J. B., Kenyon, J. S., Djalalova, I., Bianco, L., Turner, D. D., Pichugina, Y., Choukulkar, A., Toy, M. D., Brown, J. M., Angevine, W. M., Akish, E., Bao, J., Jimenez, P., Kosovic, B., Lundquist, K. A., Draxl, C., Lundquist, J. K., McCaa, J., McCaffrey, K., Lantz, K., Long, C., Wilczak, J., Banta, R., Marquis, M., Redfern, S., Berg, L. K., Shaw, W., and Cline, J.: Improving Wind Energy Forecasting through Numerical Weather Prediction Model Development, Bulletin of the American Meteorological Society, 100, 2201–2220, 2019.

Paulsen, J., Schneemann, J., Steinfeld, G., Theuer, F., and Kühn, M.: Low-level jets' influence on the power conversion efficiency of offshore wind turbines, Wind Energy Science, 11, 321–346, https://doi.org/10.5194/wes-11-321-2026, 2026.

Platis, A., Hundhausen, M., Lampert, A., Emeis, S., and Bange, J.: The Role of Atmospheric Stability and Turbulence in Offshore Wind-Farm Wakes in the German Bight, Boundary-Layer Meteorology, 182, 441–469, https://doi.org/10.1007/s10546-021-00668-4, 2022.

Quint, D., Lundquist, J. K., Bodini, N., and Rosencrans, D.: Simulated meteorological impacts of offshore wind turbines and sensitivity to the amount of added turbulence kinetic energy, Wind Energy Science, 10, 1269–1301, https://doi.org/10.5194/wes-10-1269-2025, 2025.

Robey, R. and Lundquist, J. K.: Behavior and mechanisms of Doppler wind lidar error in varying stability regimes, Atmospheric Measurement Techniques, 15, 4585–4622, https://doi.org/10.5194/amt-15-4585-2022, 2022.

Rosencrans, D., Lundquist, J. K., Optis, M., Rybchuk, A., Bodini, N., and Rossol, M.: Seasonal variability of wake impacts on US mid-Atlantic offshore wind plant power production, Wind Energy Science, 9, 555–583, https://doi.org/10.5194/wes-9-555-2024, 2024.

Sathe, A., Gryning, S. E., and Peña, A.: Comparison of the atmospheric stability and wind profiles at two wind farm sites over a long marine fetch in the North Sea, Wind Energy, 14, 767–780, 2011.

Sathe, A., Mann, J., Barlas, T., Bierbooms, W., and Van Bussel, G.: Influence of atmospheric stability on wind turbine loads, Wind Energy, 16, 1013–1032, https://doi.org/10.1002/we.1528, 2013.

Schneemann, J., Theuer, F., Rott, A., Dörenkämper, M., and Kühn, M.: Offshore wind farm global blockage measured with scanning lidar, Wind Energy Science, 6, 521–538, https://doi.org/10.5194/wes-6-521-2021, 2021.

Shaw, W., Berg, L., Debnath, M., Deskos, G., Draxl, C., Ghate, V., Hasager, C., Kotamarthi, R., Mirocha, J., Muradyan, P., Pringle, W., Turner, D., and Wilczak, J.: Scientific Challenges to Characterizing the Wind Resource in the Marine Atmospheric Boundary Layer, Wind Energy Science, pp. 2307–2334, https://doi.org/10.5194/wes-7-2307-2022, 2022.

Shaw, W. J., Berg, L. K., Cline, J., Draxl, C., Djalalova, I., Grimit, E. P., Lundquist, J. K., Marquis, M., McCaa, J., Olson, J. B., Sivaraman, C., Sharp, J., and Wilczak, J. M.: The Second Wind Forecast Improvement Project (WFIP2): General Overview, Bulletin of the American Meteorological Society, 100, 1687–1699, https://doi.org/10.1175/BAMS-D-18-0036.1, 2019.

Stull, R. B., ed.: An Introduction to Boundary Layer Meteorology, Springer Netherlands, Dordrecht, ISBN 978-90-277-2769-5 978-94-009-3027-8, https://doi.org/10.1007/978-94-009-3027-8, 1988.

Vallis, G. K.: Atmospheric and Oceanic Fluid Dynamics: Fundamentals and Large-Scale Circulation, Cambridge University Press, 2 edn., ISBN 978-1-107-06550-5 978-1-107-58841-7, https://doi.org/10.1017/9781107588417, 2017.

Vasquez-Barros, V.: BargeStabilityDecoupling, https://github.com/valeria-vasquez-barros/BargeStabilityDecoupling, 2026.

Wilczak, J., Finley, C., Freedman, J., Cline, J., Bianco, L., Olson, J., Djalalova, I., Sheridan, L., Ahlstrom, M., Manobianco, J., Zack, J., Carley, J. R., Benjamin, S., Coulter, R., Berg, L. K., Mirocha, J., Clawson, K., Natenberg, E., and Marquis, M.: The Wind Forecast Improvement Project (WFIP): A Public–Private Partnership Addressing Wind Energy Forecast Needs, https://doi.org/10.1175/bams-d-14-00107.1, iSSN: 10 Volume: 96, 2015.

Wilczak, J. M., Stoelinga, M., Berg, L. K., Sharp, J., Draxl, C., McCaffrey, K., Banta, R. M., Bianco, L., Djalalova, I., Lundquist, J. K., Muradyan, P., Choukulkar, A., Leo, L., Bonin, T., Pichugina, Y., Eckman, R., Long, C. N., Lantz, K., Worsnop, R. P., Bickford, J., Bodini, N., Chand, D., Clifton, A., Cline, J., Cook, D. R., Fernando, H. J., Friedrich, K., Krishnamurthy, R., Marquis, M., McCaa, J., Olson, J. B., Otarola-Bustos, S., Scott, G., Shaw, W. J., Wharton, S., and White, A. B.: The Second Wind Forecast Improvement Project (WFIP2): Observational Field Campaign, Bulletin of the American Meteorological Society, 100, 1701–1723, https://doi.org/10.1175/BAMS-D-18-0035.1, 2019.

Xia, G., Optis, M., Deskos, G., Sinner, M., Mulas Hernando, D., Lundquist, J. K., Kumler, A., Sanchez Gomez, M., Fleming, P., and Musial, W.: Understanding Cluster Wake-Induced Energy Losses off the U.S. East Coast, Wind Energy Science Discussions, pp. 1–35, https://doi.org/10.5194/wes-2025-154, 2025.

Zippel, S.: Eddy Covariance Flux / Processed Data., https://wdh.energy.gov/data/wfip3/barg.ecflux.z01.a0, 2026.